

Contents lists available at ScienceDirect

Tectonophysics

journal homepage: www.elsevier.com/locate/tecto



Variable source depth beneath the Indian Ocean geoid low area: Insights from L_1 and L_2 norm-based scaling power spectrum inversion

Shib Sankar Ganguli*, Prakash Kumar, V.P. Dimri

CSIR-National Geophysical Research Institute, Uppal Road, Hyderabad 500007, Telangana State, India

ARTICLE INFO

Keywords: Indian Ocean geoid low Scaling power spectrum Source depth $L_1\text{-}L_2$ norm inversion Upper mantle

ABSTRACT

Indian Ocean geoid low, situated at the south of the Indian peninsula, is an intriguing feature. Hitherto, several interpretations have been put forth to explain the genesis and causative depths of the anomaly. In this work, we investigate the scaling spectral inversion approach utilizing gravity data to estimate the causative depth and nature of the source from this region. In practice, crustal or sub-surface heterogeneities follow scaling or fractal characteristics, and comparative studies across various regions suggest that the scaling power spectrum method provides better insights into the sub-surface source distribution. An optimum fitting and comparison between the modeled and observed power spectrum have been attained by utilizing two norm penalties e.g. L1 and L2 norms for various combinations of depth and scaling exponents. Equally important, the L₁ norm misfit function yields better results when compared to the L2 norm function. We propose that estimated source depths (80 km and 120 km, respectively) are perfect examples of a half-space model with a source following scaling or fractal characteristics (scaling exponent value of-1.78) along the upper mantle boundary. However, the scaling spectrum windowing analysis of the studied region reveals a variable depth to long wavelength sources as 1014 km, 431 km, and 94 km, which conform well with the recently published depth range. Further, the weight of low and high wavenumbers indicates that the causative source depths might be due to the above-stated depth range rather than a single model fit. The study has demonstrated a good case for wider use of L₁ norm-based power spectrum inversion for source depth estimation from potential field data. We further suggest that the causative source for the Indian Ocean geoid low may extend deeper than upper mantle discontinuities.

1. Introduction

Spectral analysis of potential field data to infer depths of geologic features in sedimentary basins has been used widely for the past few decades. This method is based on modeling the source distributions of a statistical block ensemble of simple bodies, such as prisms buried at a specific depth (Bhattacharyya, 1964; Spector and Grant, 1970; Connard et al., 1983; Negi et al., 1987 and several others) and other source geometries including needle-shaped bodies with random and uncorrelated constant magnetization (Naidu, 1972; Garct'a-Abdeslem and Ness, 1994; Ross et al., 2006), or randomly distributed equivalent-source density layer (Dampney, 1969; Pawlowski, 1994; Oliveira Jr. et al., 2013). The depth to the source consistently governs the basis of the radially averaged power spectrum (RAPS) of the potential field data (Spector and Grant, 1970; Reid et al., 1990). In this case, 'radially averaged' refers to an average of the powers over the specific wavenumbers of a spectral window. It is to be realized that this approach is inherently biased since

it provides a power spectrum that involves a lot of power from the grid tapering outside of the data spectrum to satisfy edge matching. A significant quantity of power may leak into the neighborhood of low frequency, much of which can be sidestepped by eliminating the slowly varying components by means of subtracting a least-squares polynomial or by low pass filtering. In a 2D plane of observation, the RAPS of the potential field exhibit a declining trend with an increase in depth to a source in an exponential manner i.e. exp.(–2df), d and f being the depth and wavenumber, respectively. In such a means, the depth to the source might be obtained from the slope of the log of the radially averaged power spectrum.

Despite its wide applications in the interpretation and processing of potential field data, the spectral analysis tool offers limitations due to the inherent assumption of stationary and uncorrelated, purely random distribution of source geometries (Maus and Dimri, 1995, 1996; Quarta et al., 2000; Bansal and Dimri, 2001). In practice, such an assumption works for mathematical simplicity and may not replicate the natural

E-mail address: shibg@ngri.res.in (S.S. Ganguli).

^{*} Corresponding author.

behavior of a source. A more realistic approach was introduced by Mandelbrot (1982) to estimate the power spectral density of various physical properties in nature. Later, Pilkington and Todoeschuck (1990) demonstrated the efficacy and validity of this approach to understand the power spectra of various geophysical parameters (e.g. acoustic, density, resistivity, gamma-ray, etc.) and confirmed that these variables remarkably follow a scaling law. In such a strategy, to estimate the depth to source, scaling behavior of source distribution, an attribute of fractals, whose power spectral density is proportional to f^{β} (f = wave number and β = scaling exponent), is considered. Essentially, the scaling exponent, β , characterize the proportion of long and short wavelength variations of an anomaly. In the case of potential field studies, Gregotski et al. (1991) were the first to apply a scaling approach to aeromagnetic data of the North American continent to delineate lithologies. Subsequently, several workers have utilized the scaling spectral method (SSM) for potential field data processing and interpretations (Turcotte, 1992; Pilkington and Todoeschuck, 1993; Maus and Dimri, 1994, 1995, 1996; Fedi et al., 1997; Lovejoy et al., 2001; Ganguli and Dimri, 2013; Chen et al., 2015, 2016; Fedi, 2016; Dimri and Ganguli, 2019).

The geoid i.e. the gravitational equipotential surface is directly linked to the density distribution and rheology of the earth's interior. Several hypotheses on the genesis of geoid anomaly have been put forward by numerous researchers based on various geophysical observations. Quite many workers proposed that variations in viscosity due to phase change or chemical heterogeneity are one of the major causes of long wavelength geoid anomalies (Hager, 1984; Ricard et al., 1984; Hager and Richards, 1989; Steinberger, 2000; Čadek and Fleitout, 2006; Steinberger and Calderwood, 2006; Shahraki et al., 2015). While, others have suggested the occurrence of low geoid anomaly is due to the palaeo-subduction and low-density mantle upwellings (Chase and Sprowl, 1983; Hager and Richards, 1989; Richards and Engebretson, 1992; Spasojevic et al., 2010; Rudolph et al., 2015). However, a decisive elucidation about the genesis of the extreme negative geoid anomaly of the enigmatic Indian Ocean geoid low (IOGL) is still a scientific puzzle. The undulation at the core-mantle interface has also been put forth as a causative mechanism for the IOGL (Negi et al., 1987). Further, to elucidate the strong negative geoid anomaly, numerous workers have propounded other theories such as the presence of low dense subducted rocks of the Tethyan lithosphere within the mid-to-upper mantle (Mishra, 2014; Mishra and Ravi Kumar, 2012), unindemnified depression in the upper mantle (Ihnen and Whitcomb, 1983), the existence of slab dehydration at the mid-to-upper mantle depths (Rao and Kumar, 2014; Rao et al., 2020), and due to a long-lasting back-arc basin south of Eurasia's paleomargin (Nerlich et al., 2016). Based on SS and PP precursors, Reiss et al. (2017) postulated that joint consequence of hot mantle material in the midmantle beneath the IOGL and cold dense rocks below 660 km beyond the south gave rise to such striking geoid low. Additionally, Ghosh et al. (2017) concluded that the IOGL is due to the density-driven mantle convection possibly originating from the edge of the African Large Low Shear Velocity Province (LLSVP). Most recently, Steinberger et al. (2021) demonstrated that IOGL can be explained by the overlay of two approximately orthogonal geoid troughs, one trough due to cold slabs in the lower mantle and the other due to hot material in the upper mantle.

The gravity inverse problem is inherently non-unique and obtaining a stable, geologically meaningful solution becomes feasible with the minimization of the objective or cost function, namely a function that quantifies how far the predicted values are from the observed values. There are several choices for the solution norm penalty (stabilizer) to minimize the objective function (Dimri, 1992). L_2 norm is the most widely used norm penalty to stabilize the solution and recover the desired model. Nevertheless, it imposes smoothness on the estimated model, which leads to blurred models (Utsugi, 2019). In recent years, with the dawn of compressive sensing, the use of the L_1 norm in parameter estimation has been gaining popularity since it is not sensitive to outliers and yields focused sparse models. Yet, the application of the

 L_1 norm function to estimate depth using scaling power spectrum analysis has not been tested widely, except by Maus and Dimri (1996). Moreover, source depth estimation in the Indian Ocean geoid low area using gravity data has not been extensively studied. Mishra and Ravi Kumar (2012) reported such depth analysis and that too based on power spectral analysis without taking into consideration of scaling approach, which is subjected to estimation error of about 10–15%. Consequently, we believe that there is ample scope to testify and compare the performance of both L_1 and L_2 norm penalties while inverting the scaling power spectrum to estimate the depth to the causative source beneath this spectacular geoid low region. In the following, we examined the application of L_1 and L_2 norm-based scaling spectral method for depth estimation problems to the gravity data collected from the Indian Ocean geoid low region, south of the Indian peninsula and Sri Lanka, and feasible inferences were drawn in terms of mantle deep-seated bodies.

2. Concept of L1 and L2 norm-based scaling spectral method

The 3D spectral density of a source distribution following fractal or scaling behavior and comprising isotropic scaling exponent $= \beta$ can be represented in the form of (Maus and Dimri, 1996)

$$F(u,v,w) = C_s \left\lceil \sqrt{u^2+v^2+w^2} \right\rceil^{-\beta} \tag{1} \label{eq:force}$$

where C_s is a constant term representing the strength of the causative source variations and u, v and w define the x, y, and z-component of the wavevector, respectively. The power spectral density of a gravity field in a horizontal plane of observation can be obtained by solving the following equation (for details, please refer to Maus and Dimri, 1994):

$$F_g(u,v) = C_\rho^2 C_s \int w^2 / |K|^4 \Big(\sqrt{u^2 + v^2 + w^2} \Big)^{-\beta} dw = C_g S^{-(\beta+1)} \tag{2} \label{eq:2}$$

where K is the wavevector, $S=\sqrt{u^2+v^2}$ and C_g , C_ρ are constant. Note that C_g comprises the model parameters of the gravity source distribution.

It is important to note that the derived spectral density, as represented by Eq. (1), becomes infinite for any value of the isotropic scaling exponent, leading to one of the limitations of its application. However, this can be avoided by treating the spectral densities satisfying Eq. (1) but within a limited (finite) band of wavenumbers (Maus and Dimri, 1996).

A more generalized model of power spectra of the gravity field (P_d) can be obtained by the upward continuation of the gravity field from the surface of half-space to the plane of observation, in the following form

$$P_{d}(S) = C_{g}e^{-2ds}S^{-\gamma}$$
(3)

which can also be represented as

$$lnP_{d}(S) = lnC_{g} - 2dS - \gamma lnS$$
(4)

where $\gamma=\beta+1$ is the isotropic 2D scaling exponent of the gravity field, β is that of the 3D density (source) distribution, d is the depth to the causative source and S defines the absolute magnitude of the 2D wavevector. This relationship indicates that the gravity field in the observation plane due to the isotropic scaling source also obeys scaling law and may not be exact always. It is important to note that the power spectrum density in Spector and Grant's approach is constant at the source level, which is a special case of Eq. (3) when $\gamma=0$. In such a case, the radially averaged power is assessed before taking the logarithm, depicting asymmetric power distribution. On the contrary, the scaling approach considers the logarithm of the power for a constant length of the wavevector, which is symmetric and provides meaningful information. Fig. 1 illustrates the benefits of using the average of the logarithms instead of just taking the logarithm of the average. Eq. (4) suggests that the power spectrum is in a linear relationship with the model parameters

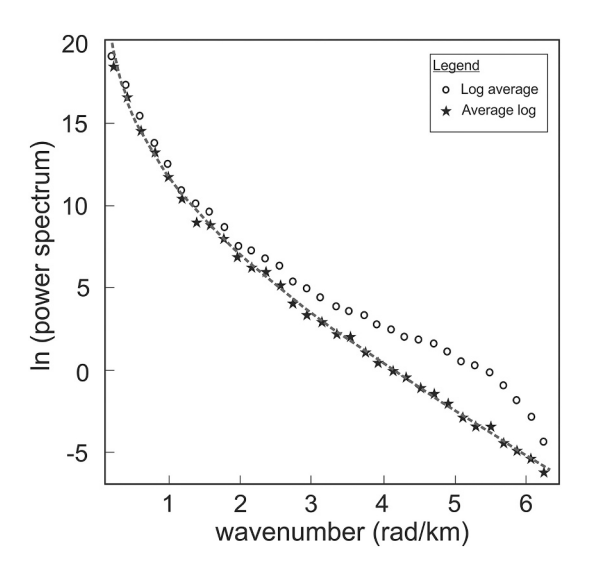


Fig. 1. Power spectrum density representation of a synthetic gravity field together with the theoretical scaling power spectrum having scaling exponent value of β =3 (dashed line). The observation plane is considered at a height of 1 km above a scaling density distribution with β =3 (after Maus and Dimri, 1995).

hence, we will be dealing with a linear inverse problem.

To finalize the model (to be determined), the misfit function will be realized by the difference between the model power spectrum and the power spectrum calculated from the observed (real) data. A typical form of the global objective function ($O^{\alpha}(m)$) can be expressed as (Menke, 2012)

$$O^{\alpha}(m) = \varphi_d(m) + \alpha R(m) \tag{6}$$

where, m, $\varphi_d(m)$, R(m), α represents the model parameters, data misfit, regularization term and regularization parameter, respectively. In general, the data misfit term deals with how well the estimated data imitate the observed (measured) one concerning a norm penalty. Further Eq. (5) can also be expressed as

$$\begin{split} O^{\alpha}(m) &= ||r||_{p} + \alpha R(m) \\ &= \left[\sum_{i=1}^{N} |D_{i} - \sum_{j} g_{ij} m_{j}|^{p} \right]^{1/p} + \alpha \left[\sum_{j=1}^{M} |m_{j} - m a_{j}|^{p} \right]^{1/p} \end{split} \tag{6}$$

Here, D_i is the measured data corresponding to N data points; m_j and ma_j are model vector w.r.t. M points and initial model; g_{ij} ($g \in R^{N \times M}$) is the sensitivity matrix resulting from the discretization of a forward modeling operator and p is the norm. The two misfit functions i.e. L_1 and L_2 norm penalties of the solution, as used in this study, can be represented in the following form:

$$L_{1}\left(\gamma,d,lnC_{g}\right) \textit{norm} = \sum_{S=0}^{W} \left|lnP_{d}(S)^{measured} - \left(lnC_{g} - 2dS - \gamma lnS\right)\right| \tag{7}$$

$$L_{2}\left(\gamma,d,lnC_{g}\right)\textit{norm} = \sum_{S=0}^{W} \left[lnP_{d}(S)^{measured} - \left(lnC_{g} - 2dS - \gamma lnS\right)\right]^{2} \tag{8}$$

These two norms provide information to have a better understanding of the optimization that can quantify how reliable are the model parameters concerning the observed power spectrum of the gravity field. The optimum model parameter triplet (γ , d, lnC_g) will be obtained by inverting the power spectrum that satisfies the global minimum values of the triplet.

3. Application to the Indian Ocean geoid and gravity low area

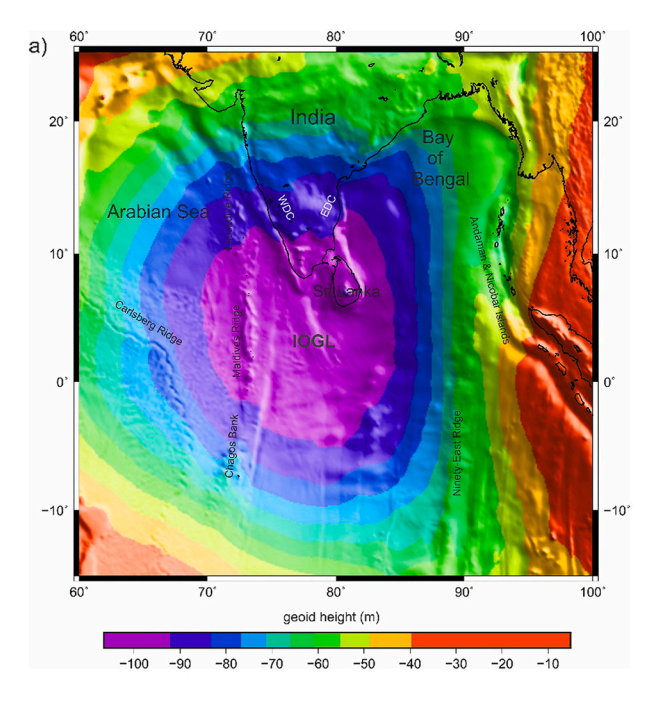
The study area, IOGL, is situated in the south of the peninsular of

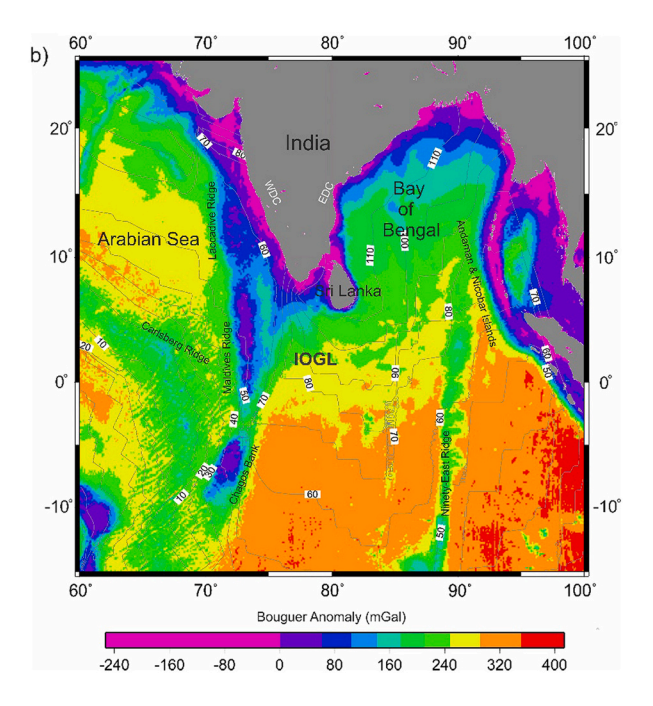
India and Sri Lanka (Fig. 2), which reflects surprisingly low gravity and geoid values. The region encompasses several complex structural features, seamounts, and magmatic processes within active and passive margins. The geoid anomaly, as deduced by removing mean dynamic topography, appears to be as low as about -106 m with its center at 3° N, 78°E (Fig. 2a). The Bouguer gravity data were derived from the latest global combined gravity field model i.e. EIGEN-6C4 including satellite GOCE data, as illustrated in Fig. 2b together with the lithospheric age. The Bouguer gravity data reveals long-and short-wavelength anomalies that vary between about -250 mGal and 410 mGal. The present geopotential model is based on the spherical harmonic calculation (based on the WGS 1984 reference system) of the Earth's gravitational field up to degree and order 2190. Note that this gravity field is highly preferred since it is inferred from the amalgamation of various satellites e.g. LAGEOS (Laser Geodynamics Satellites), GRACE (Gravity Recovery and Climate Experiment), GOCE (Gravity Field and Steady-State Ocean Circulation Explorer), and DTU10 terrestrial data (a combination of the EGM2008 global model over the continents and altimetry data over the oceans), and performs better compared to the global EGM2008 model (Förste et al., 2014).

The origin of the spectacular geoid low is believed to be due to long wavelength deep-seated sources (Negi et al., 1987; Ghosh et al., 2017), which is very difficult to realize from the complete Bouguer data, as indicated by Fig. 2b. Most importantly, deep features are masked as compared to shallow oceanic and continental tectonic features, which are more prominent. Hence, for the present study, we decided to utilize the high-resolution $(1^0 \times 1^0)$ regional gravity anomaly from this area, which ranges between -10 mGal and -42 mGal (Fig. 3). The regional field was obtained by separating (gentle cut) the 8 o to 10 o harmonic from the complete spherical harmonics of degree and order 2190. To obtain the best values of the model triplet (γ , d, lnC_g) using L₁ and L₂ norm penalties for source depth estimation, we opted for the overlapping windowing strategy involving a window size (w in Fig. 3) of 32 ° imes 32 $^{\rm o}$ (3552 imes 3552 km), moving along both east-west and north-south with a 4 $^{\rm o}$ (444 \times 444 km) step, and a 3300 km long east-west profile (indicated by a white line in Fig. 3) within the regional gravity field. The selection of window size is critical to acquiring geologically relevant results from the radially averaged spectrum analysis of potential field data (Pilkington and Todoeschuck, 1993; Fedi et al., 1997; Quarta et al., 2000). Although there exist several choices, a recent sensitivity study on the window size indicates that a window size having three to five times the expected source depth is sufficient to provide geologically meaningful information about a region (Kelemework et al., 2021). In the present study, the 2D radial scaling spectra in the Fourier domain for each subregion with overlapping window were utilized to obtain the average depth of the gravity sources in the studied region. To understand the source distribution and depth estimation, a suitable range of wavenumbers was identified through visual inspection of the segments and the least square linear fitting to the nearly linear features was performed to obtain the slopes for depth values. Further, based on the various combinations of the model triplet (γ, d, lnC_g), model power spectra are estimated to compare those with the measured power spectrum from the regional gravity data using L₁ and L₂ norm penalties. The model with minimum misfit is considered to be the final model that can reasonably explain the observed power spectrum. The data from the IOGL region, used here, provides an opportunity to check the efficacy and understand the performance of L₁ and L₂ norm functions in scaling power spectral inversion and find out the optimum model parameters to explain the causative sources.

4. Results and discussion

From the 2D radially averaged spectrum of the gravity anomaly, the log/log plot of the power spectra yielded the isotropic scaling exponent of the gravity field (γ) to be 2.78, from which the scaling exponent of the 3D scaling density (source) distribution is derived as 1.78, as shown in





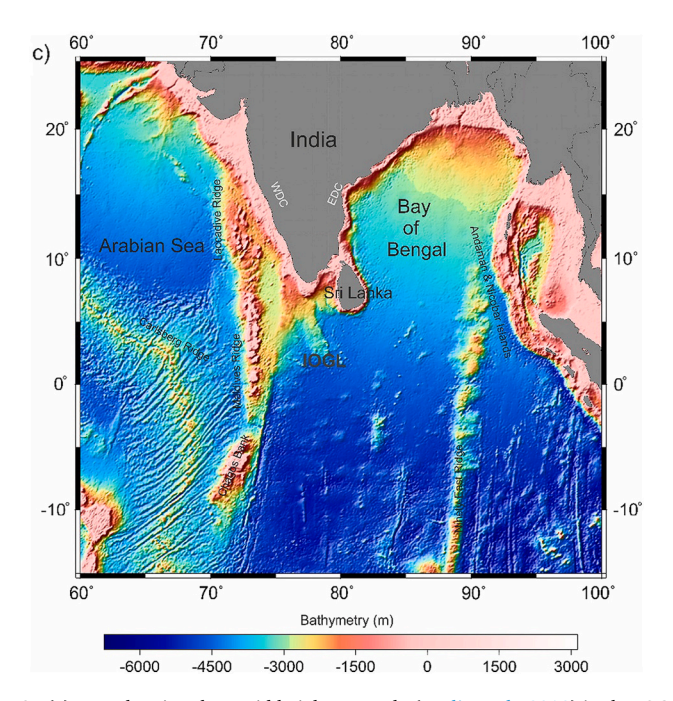


Fig. 2. (a) Map showing the geoid height anomaly (Pavlis et al., 2012) in the IOGL region, south of peninsular India. The striking geoid low (-106 m) is represented by purple colour at the adjoining area of the center i.e. 3°N, 78°E. (b) Illustration of the satellite-derived Bouguer gravity anomaly (Förste et al., 2014) together with contours of the age of the oceanic lithosphere (Ma) and the surface manifestation of the tectonic elements, and (c) bathymetry map (Smith and Sandwell, 1997) in the IOGL and adjoining areas. (For interpretation of the references to colour in this figure legend, the reader is referred to the web version of this article.)

Fig. 4. It is worth mentioning that the scaling spectral behavior of the studied gravity field exhibits the power-law scaling decay (having power-law dependencies over wide ranges of both vertical and horizontal scale) with a logarithm of wavenumber (see Fig. 4).

To obtain the optimum values of the scaling exponent together with the depth to the source, we compared the measured power spectrum of the gravity profile with the modeled one, as defined by Eq. (4). Both L_1 and L_2 norm misfit functions were realized for comparing these two power spectra. The solutions obtained from these two norm misfits for various combinations of depth and γ values are illustrated as a 2D cross-section in Fig. 5. Accordingly, for each combination, the constant

parameter, $\ln C_g$ has been optimized (see Table 1). Comparatively, the L_1 norm misfit function performed better than the L_2 norm criteria, which is given in Table 1. It is, however, striking that although the scaling power spectral inverted depth values (about 80 km and 120 km) are close to (within the range) but not directly corroborated with the depth values reported by Ghosh et al. (2017) signifying the low-density anomalies, namely in the depth range of 300 km to 900 km. Relating the geology of this region, which comprises mainly igneous and metamorphic rocks, indicates this study as a classic case of a half-space source characteristics with heterogenous and complex statistical properties of density distribution in the area. A similar case example was reported by

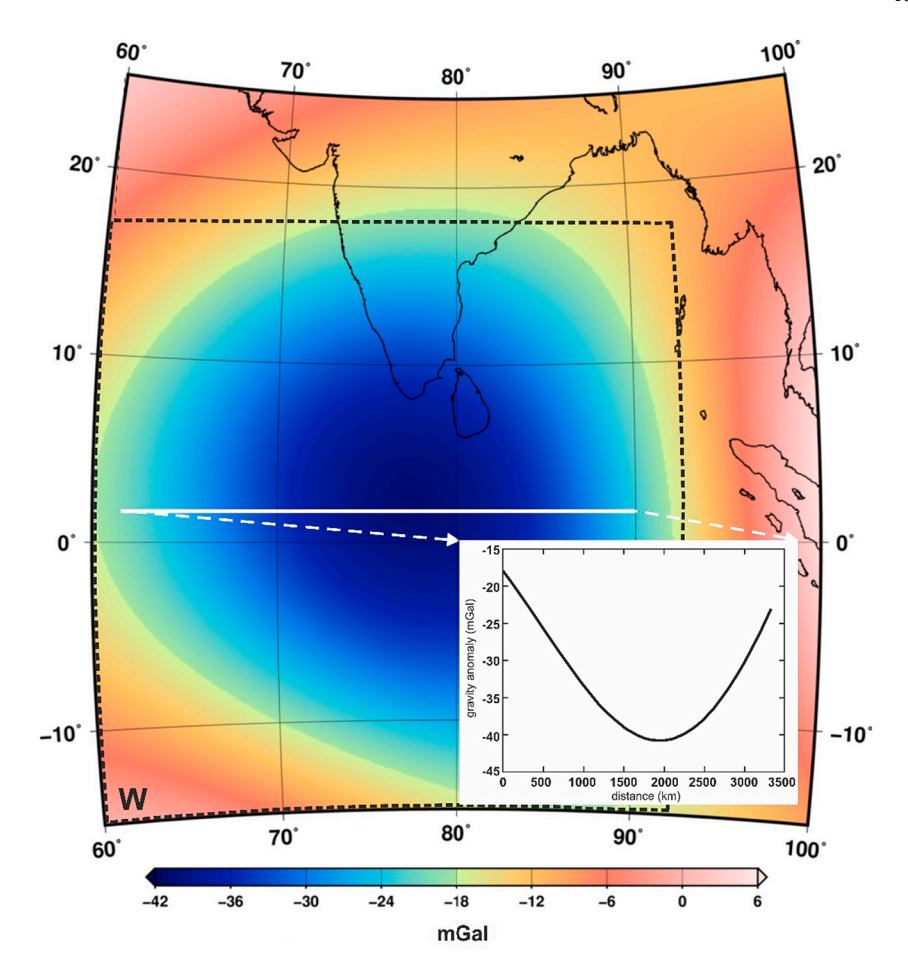


Fig. 3. Regional gravity anomaly (derived from the EIGEN-6C4 model (Foerste et al., 2014)), showing the long wavelength features of spherical harmonics of the Earth's gravitational field from the IOGL region. The black dashed area and the white line represent the square window (w, which comprises 3552 km side and 444 km shift) and a 3300 km long gravity profile used for the present study.

Maus and Dimri (1996), where consideration of a source-free top layer was suggested to obtain depth values other than that represented by the half-space layer. Most conceivably, in the present study, the optimum depth estimated using the scaling power spectral inversion reflects the depth to the surface of a half-space limited to the lithosphereasthenosphere boundary (widely referred to as LAB). This thin lithospheric characteristic (80 km) of the IOGL, which thickens progressively and attains the value of 120-132 km adjacent to the Bay of Bengal region, is in good agreement with similar findings reported recently by Gokul et al. (2022). This combined with the fact of obtaining γ magnitude of about 2.78 suggests the depth to the source could be due to mantle plumes or rising hot rocks in the upper to the mid mantle with considerable lateral extents. In general, the average y for subsurface density distribution of igneous and sedimentary rocks falls within the range of 2.0 to 2.2 (Pilkington and Todoeschuck, 1993; Dimri and Bansal, 2021). The scaling exponent for 3D density distribution, as obtained in this study, is 1.78, indicating a heterogeneous nature of the source controlled by various rock types and mantle plumes. The lower and higher ranges of scaling exponents of sources indicate tectonically stable and unstable areas, respectively (Dimri and Bansal, 2021). The tectonic framework of the studied region is thought to be associated with a significant reworking of crustal blocks since the Late Pliocene including several aseismic ridges (Schlich, 1982; Suo et al., 2021), which supports our interpretation strongly. Consequently, it would be interesting to analyze the observed power spectrum divided into different segments with this a priori information.

A proper scaling exponent is critical to infer source characteristics and depth estimation, and the assumption of an isotropic exponent may

lead to conspicuous ambiguity in selecting the correct one. Although several non-linear inversion methods have been utilized to simultaneously estimate the depth and scaling exponent, as is the case in the present study, however, it becomes often challenging to accurately estimate both the parameters since these are largely interconnected to each other (Bouligand et al., 2009; Kelemework et al., 2021). Moreover, the exponent value is heavily dependent on the method implemented to derive the power spectra (e.g. maximum entropy, Fourier, etc.) or on the window functions (Quarta et al., 2000). The estimated depth and β values can be judged based on how adequately these values explain the gravity field and the associated density distribution from the studied region. For example, error from the radial averaging process may propagate into the model leading to ambiguous results (Maus and Dimri, 1995). This can be severe even for small grid spacing. Furthermore, the derived model will assume a constant scaling exponent for the entire source distribution, which is nothing but an approximation of the statistical properties of the density distribution. Note that the scaling exponent of the subarea or segment may differ from the entire survey area. It is worth mentioning that, despite using only a model triplet comprising γ , d, and lnC_g , the modeled power spectrum seems to be very well fitted to the measured spectrum of the gravity field, except for a few points, as indicated in Fig. 6. This is one of the significant advantages of this method for a meaningful understanding of the source distribution. The best fit model referred to here signifies a model with optimum parameters that explain the non-linear field meticulously.

As mentioned earlier, we divided the gravity map into overlapping windows and estimated the radially averaged power spectra following scaling relations to infer meaningful information about the depth of the

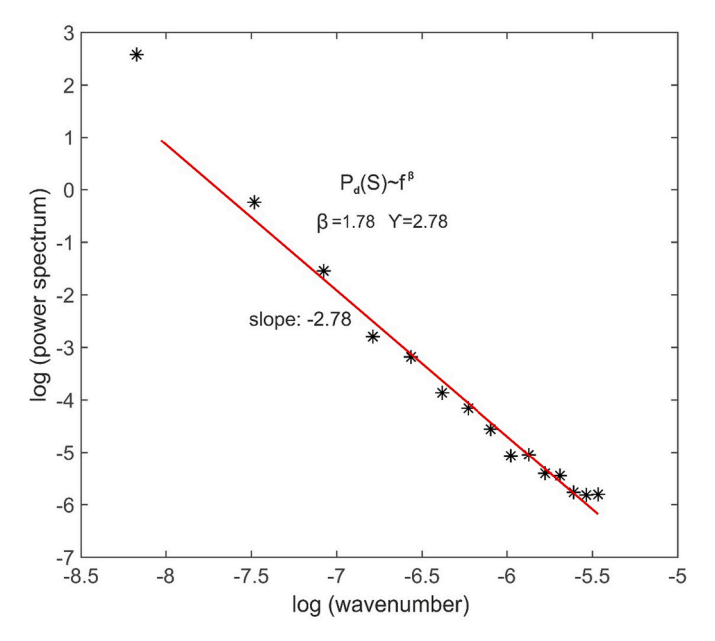
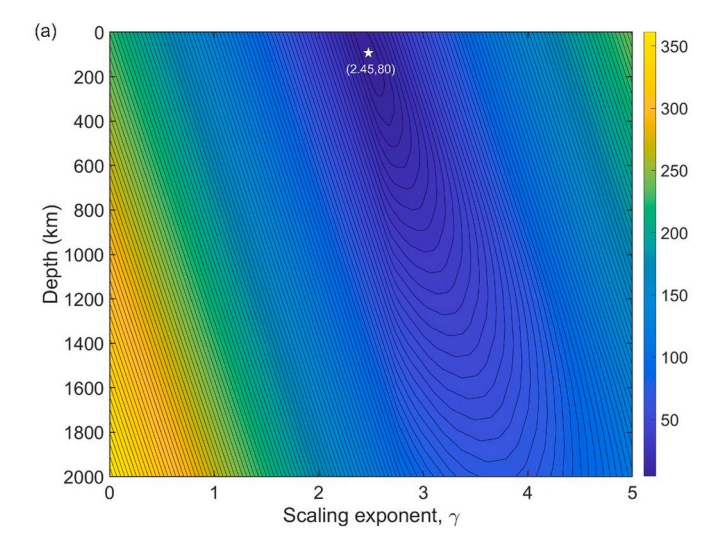


Fig. 4. Evaluation of scaling exponent of the source distribution for gravity data gridded at 1° deg. interval (see Fig. 3). The red curve represents the fit of the 2D radially averaged log power spectra obtained from the overlapping windows to obtain the value of β =1.78. (For interpretation of the references to colour in this figure legend, the reader is referred to the web version of this article.)

causative sources in the IOGL region. Further, through visual examination, a range of wavenumbers namely 0.002< S <0.008 rad/km is decided to obtain a linear slope for deeper depth information and 0.010 < S < 0.042 rad/km for estimating intermediate to comparatively shallower depths (see Fig. 7a). Besides, the range of wavenumbers for the profile data is chosen as 0.003 < S < 0.008 rad/km for the inference of deep-seated sources and 0.008 < S < 0.028 rad/km for other depth of sources (Fig. 7b). Weightage of low and high wavenumbers together explains the spectrum extremely well for all possible depths to the causative source rather than a single model fit, where the latter is mainly due to the density stratification in the upper lithospheric level. From the $\,$ 2D radially averaged scaling power spectra, the inferred depth values range between 1014 km, 431 km, and 94 km, while the profile data reveals these source depths as 924 km, 392 km and 102 km with the average estimation error varies between ± 4.5 km for shallow sources, \pm 20 km for intermediate depths and \pm 48 km for the relatively deep origin of sources, respectively (Figs. 7a & 7b). These inferred depth values, however, resemble closely the depth range as also reported by Ghosh et al. (2017). The depth corresponding to the range of 94–102 km indicates the causative source along the lithosphere-asthenosphere boundary and coincides with the half-space model as obtained from the scaling power spectral inversion. The S-receiver functions study also shows the average thickness of the lithosphere in the Indian Ocean is in a similar range (Kumar et al., 2007). Further, to identify if there is any thermal variation in lithospheric thickness that might influence our calculation, we plotted the thickness of the oceanic lithosphere with its age, as illustrated in Fig. 8. The isotherms are computed using the GDH model given by Stein and Stein (1992). The thermal model is constructed considering the temperature at the base of the plate to be 1350 °C potential temperature. The figure shows that the age of the first 0-40 Ma appears more pronounced compared to the rest where it tends to remain nearly constant. Interestingly, the lithospheric age in and around the IOGL is in the range of 65-90 Ma (Fig. 2b). This implies that there is no significant thermal variation in lithospheric thickness which might have affected our calculation.

The inferred depth range of 392 \pm 19 km to 431 \pm 21 km suggests the depth for the upper mantle discontinuity (i.e. 410 km discontinuity



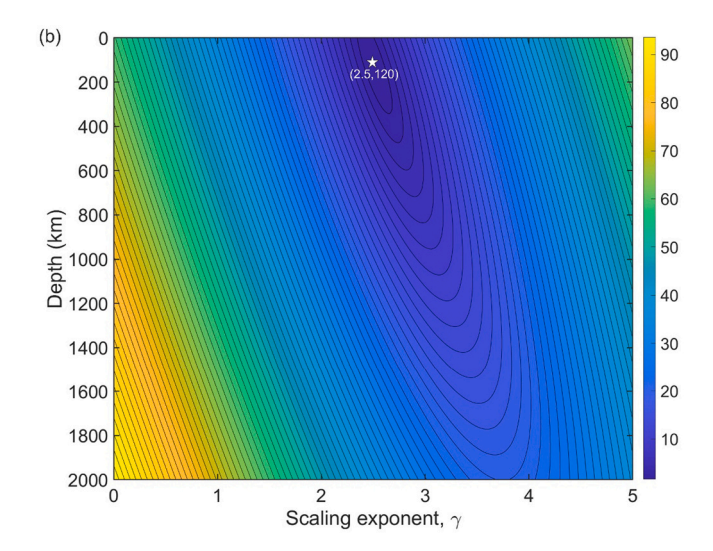


Fig. 5. Representation of the misfit functions of the modeled power spectrum using two norm penalties: (a) L_1 norm (top) and (b) L_2 norm (bottom), respectively. Here, different combinations of depth and γ were utilized to find the best fit model.

Table 1 Estimated depth, γ , and the constant lnC_g values for the studied gravity data for a window size of $32^o \times 32^o$ with a 4^o step size including the wavenumber range of 0.002 < S < 0.042 rad/km, as obtained from L_1 and L_2 norm misfit functions.

Misfit functions	Depth to source (km)	Scaling exponent of the field (γ)	Constant lnC _g
L ₁ norm	80	2.45	−19
L ₂ norm	120	2.5	−19.3

(D410) as inferred from the IASP91 earth model). We found that the D410 topography is slightly depressed, which is in accord with the reported observations of differential travel times of PP and SS waves (Reiss et al., 2017) and high-quality P to S wave radial receiver functions data acquired from the sizeable array of Ocean Bottom Seismometers (Negi et al., 2022). Such a depressed D410 topography relies heavily on the surrounding mantle temperature conditions and is attributed to a hot midmantle anomaly accompanying a thin mantle transition zone (MTZ) representing an exothermic phase transition of olivine (Ol) to the wadsleyite (Wd) (Jenkins et al., 2016; Chanyshev et al., 2022). In essence, the unusual negative Clapeyron slope at D410 conclusively indicates

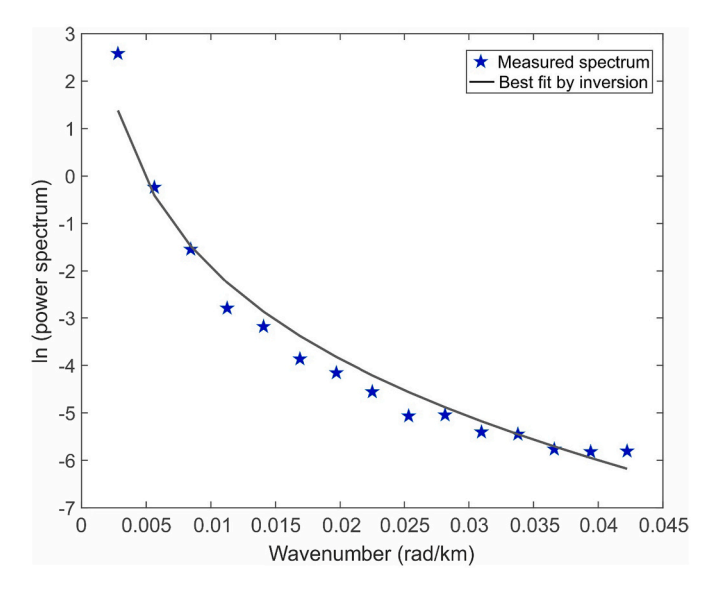
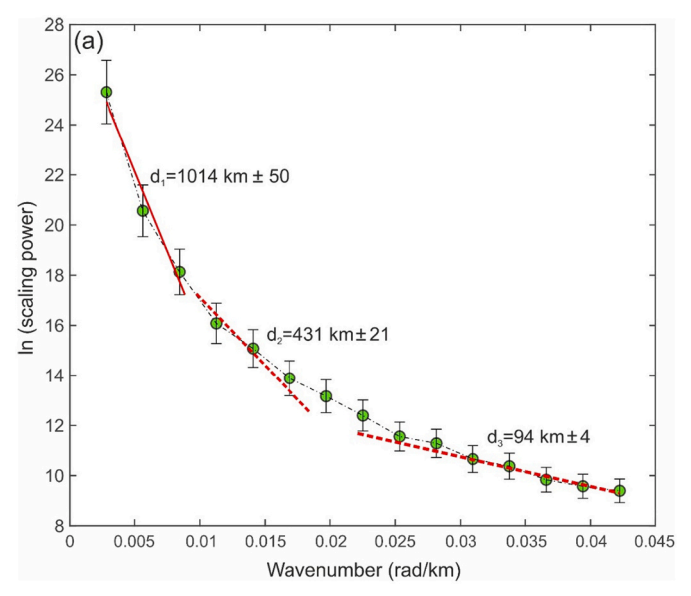


Fig. 6. Illustration of the best fit model obtained from scaling power spectral inversion of the studied gravity data.

that the MTZ is highly perturbed in the IOGL region when compared to the global mean due to the presence of hot midmantle anomalies (Negi et al., 2022). Intriguingly, these hot anomalies correspond well with the low-density (about 0.2% of the size and shape of IOGL) and low-velocity anomalies in the depth range of 300 km to 900 km beneath the IOGL (Ghosh et al., 2017; Steinberger et al., 2021). It is, however, striking that the origin of such a thermal (hot) anomaly remains elusive since there is no direct evidence of a mantle plume immediately beneath the IOGL area. A plethora of thermal anomalies has been believed to be originated in the upper mantle beneath East Africa, which further channeled from north of Madagascar towards the present location of the IOGL (Ghosh et al., 2017). Current global tomography models such as GyPSuM (Simmons et al., 2010), S40RTS (Ritsema et al., 2011), SAVANI (Auer et al., 2014), SGLOBE-rani (Chang et al., 2015) and others also reveal that low S-velocity anomalies are persistent and ascribed to hot mantle material arising from the Kenya plume and flowing towards the south of India as a part of the large scale conveyor belt (Steinberger et al., 2021) involving upwelling from the African LLSVP in the direction of the dehydrated ancient subducted slabs of the Tethyan collisional zone. Fig. 9 illustrates the vote map as derived from many seismic tomography models (Hosseini et al., 2018), which reveals the low S-velocity anomalies (orange/red colors) that coincide well with the low-density anomalies extending from the east of East Africa towards the west coast, mid-oceanic ridges and southern part of India (Ghosh et al., 2017). The fast movement of the Indian plate could have accelerated the mantle flow from East Africa to mid-oceanic ridges and the southern part of India (Kumar et al., 2007; Steinberger et al., 2021). More interestingly, the low-velocity anomalies are prominent at all mantle depths, except for depths beyond 900 km, where the high-velocities vote map is dominant, as illustrated in Fig. 9. This supports our findings that the source of the IOGL anomaly is mainly arising from variable depths in the range of 100 km to 1000 km, exhibiting the scaling behavior of the rocks (gradational density) both at the upper mantle and top part of the lower mantle. There is another argument for geoid low, which states that the coupled mechanism of high-density anomalies in the lower mantle due to ancient slab graveyards with the low-density and low-velocity materials in the upper mantle can strongly reproduce such anomalous structure (Spasojevic et al., 2010). This is also supported by the receiver function results from a few stations in and around the IOGL together with PP and SS precursor studies (Rao et al., 2020; Reiss et al., 2017).

Nevertheless, the direct evidence of gravity low due to heterogeneous density distribution remains unexplained, except for the scaling



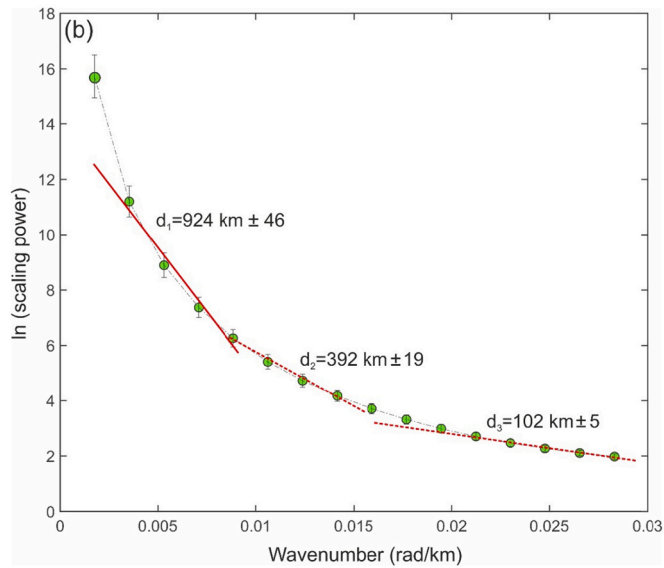


Fig. 7. Estimation of depth to the sources in the regional gravity anomaly map of the IOGL region using a window size of (a) 3552×3552 km and (b) profile data, as shown in Fig. 3. The slope represents the various depth values as obtained during the spectrum fitting. The error bars define the 95% confidence intervals for the radially averaged scaling power spectrum.

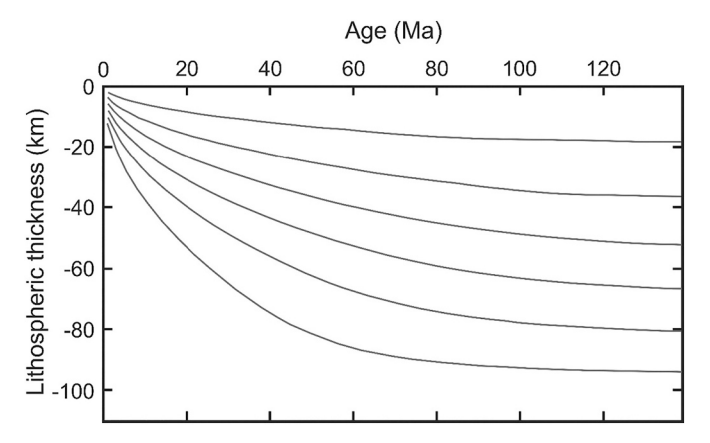


Fig. 8. Plate thicknesses of oceanic lithospheres are plotted against their age. Isotherms lines are plotted with an interval of 200 $^{\circ}$ C.

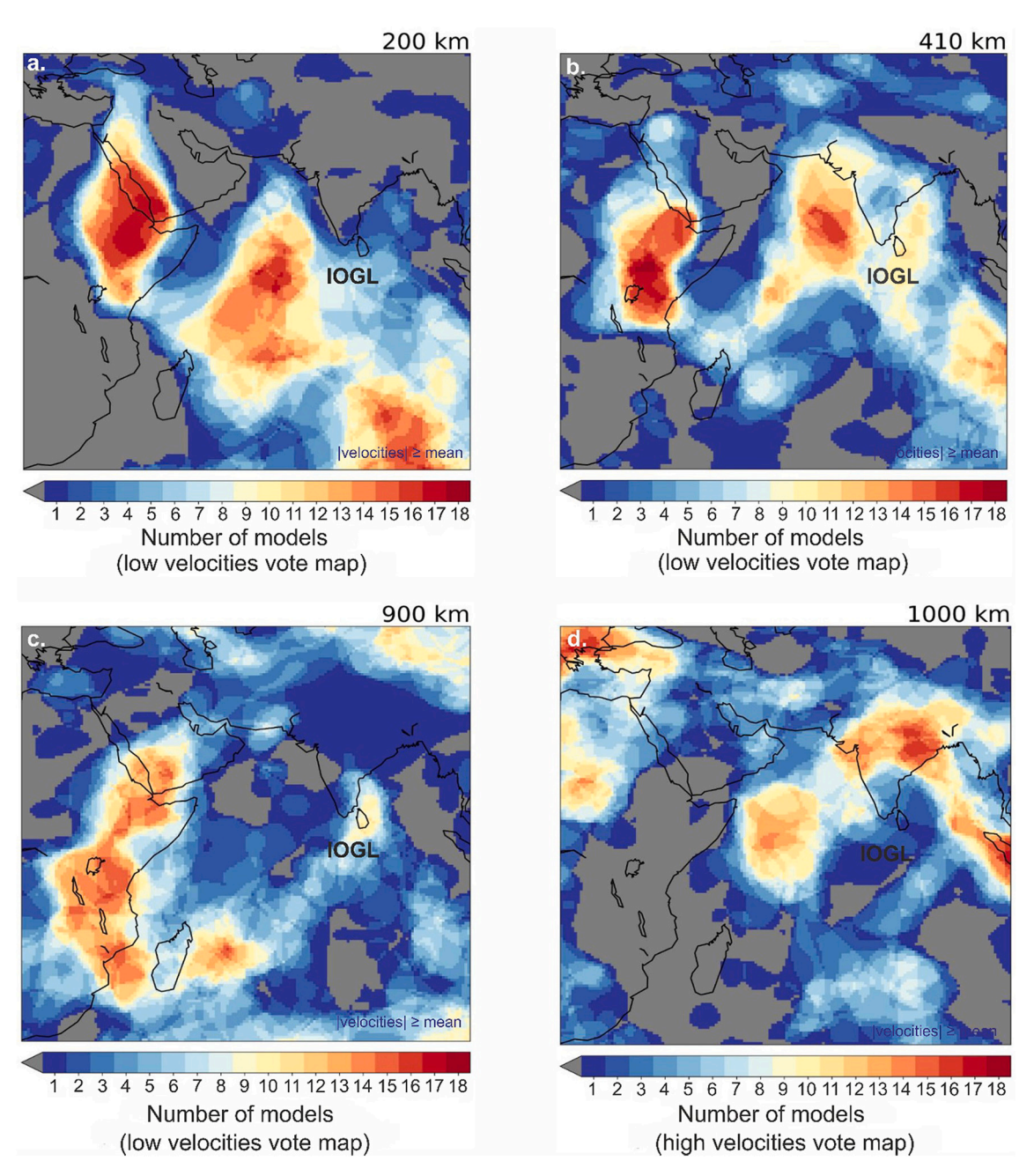


Fig. 9. Representation of vote map of all S-velocity models at various depths namely 200 km, 410 km, 900 km, and 1000 km as provided by Hosseini et al. (2018).

characteristic of the source. Our analysis clearly suggests that the source of the IOGL lies at variable depths covering mostly the upper mantle and some parts even deeper than the upper mantle transition zone, which is mineralogically interpreted as phase transitions from α -olivine to β -spinel, and from γ -spinel to perovskite+magnesiowüstite, respectively. We speculate that one of the possible origins of such extreme geoid (and gravity) anomaly is due to the gradational change (due to scaling characteristics) between low mid-to-upper mantle hot, lowdensity rocks subjected to high-grade metamorphism, and cold dense rocks at the upper part of the lower mantle. Our gravity results are in accord with the model of the deep genesis of the IOGL as suggested by Ghosh et al. (2017) and Steinberger et al. (2021), who advocate the cause of the anomaly is the material rising from the African LLSVP and moving towards the northeast. The density reduction can be explained in several ways, therefore at present, it is difficult to ascertain the exact cause of the anomaly. However, based on the accurate depth information from this study, we could ascertain that the genesis of the anomaly

may not be due to a single factor but related to several components such as LLSVP (e.g. Masters et al., 2000; Grand, 2002, and many others) and the locale of a slab graveyard (Spasojevic et al., 2010; Rao et al., 2020). The genesis and source depths of the IOGL anomaly are enigmatic and integrated modeling involving petrological, seismic, heat flow, and other observations might be useful to explain such a complex nature.

5. Conclusions

Here, we analyzed the power spectrum of the gravity field obtained from a widely known and unique geoidal low region on the Earth (i.e. Indian Ocean geoid low), and invert it to get meaningful information about the depth of a feasible source distribution. The assumption of a scaling source distribution following scaling geology is considered here. It is evident from the power spectrum analysis that the gravity field from the studied region decays by approximately f^{2.78}. Note that the scaling exponent may potentially vary with regions following different geology.

The advantage of the adopted scaling power spectral inversion method is that it does not require any impractical assumptions such as white noise or random source distribution. An optimum fit to the power spectrum was obtained by realizing two popular misfit functions i.e. L₁ and L₂norm solutions for different combinations of depth and scaling exponent values. Comparatively, the L₁ norm solution explains the model fit more accurately than L₂-norm misfit function. The depth values such as 80 km and 120 km obtained from these two approaches were attributed to a half-space model following the 3D scaling source distribution, which signifies the LAB depth and falls within the reported depth range (300-900 km) by Ghosh et al. (2017) within the upper mantle but could not explain the data alone. So, we focused our attention to analyze the gravity map into overlapping windows and dividing the observed power spectra into segments corresponding to source heterogeneities attributed from various depth levels that follow scaling geology. We found a variable feasible depth to the source from the studied region, which falls within the range of 924-1014 km, 392-431 km, and 94-102 km with the average estimation error varying between 4.5 km for shallow sources, 20 km for intermediate depths and 48 km for the relatively deep origin of sources, respectively. Our source depth findings are in accord with the low S-velocity anomalies as observed within the vote map and the published depth range, as evident from Ghosh et al. (2017). The derived results were found to be strongly dependent on the chosen window size for scaling power spectrum inversion. The model developed here, elucidates the shape and characteristics of the observed power spectrum reasonably well. It is also interesting to note that a best-fit model can only be anticipated if the scaling exponent correlates well with the surface or sub-surface geology. We propose that the origin of such an extreme geoid anomaly is attributed to the gradational density change between lower mid-to-upper mantle hot, less dense rocks subjected to high-grade metamorphism and cold dense rocks residing in the top part of the lower mantle.

CRediT authorship contribution statement

Shib Sankar Ganguli: Conceptualization, Resources, Formal analysis, Investigation, Methodology, Software, Validation, Visualization, Writing – original draft, Writing – review & editing, Funding acquisition. Prakash Kumar: Resources, Visualization, Validation, Writing – review & editing. V.P. Dimri: Project administration, Writing – review & editing.

Declaration of Competing Interest

The authors declare that they have no known competing financial interests or personal relationships that could have appeared to influence the work reported in this paper.

Data availability

Data will be made available on request.

Acknowledgments

We would like to offer our deepest gratitude to Dr. Ling Chen (Editor), Dr. Dhananjai Pandey (Handling Editor) for careful editorial handling, and two anonymous reviewers for providing constructive comments to improve the manuscript. We extend our thanks to the Director, CSIR-NGRI for all the support and for giving kind consent to publish the results. SSG would like to thank DST, Govt. of India for the DST Inspire Faculty research grant (grant no. DST/INSPIRE/04/2016/000174) utilized as financial support for this study.

References

- Auer, L., Boschi, L., Becker, T.W., Nissen-Meyer, T., Giardini, D., 2014. Savani: a variable resolution whole-mantle model of anisotropic shear velocity variations based on multiple data sets. J. Geophys. Res. 119, 3006–3034.
- Bansal, A.R., Dimri, V.P., 2001. Depth estimation from the scaling power spectral density of nonstationary gravity profile. Pure Appl. Geophys. 158 (4), 799–812.
- Bhattacharyya, B.K., 1964. Magnetic anomalies due to prism-shape bodies with arbitrary polarization. Geophys. 29, 517–553.
- Bouligand, C., Glen, J.M.G., Blakely, R.J., 2009. Mapping Curie temperature depth in the western United States with a fractal model for crustal magnetization. J. Geophy. Res. 114. B11104.
- Čadek, O., Fleitout, L., 2006. Effect of lateral viscosity variations in the core-mantle boundary region on predictions of the long wavelength geoid. Stud. Geophys. Geod. 50, 217–232.
- Chang, S.J., Ferreira, A.M.G., Ritsema, J., van Heijst, H.J., Woodhouse, J.H., 2015. Joint inversion for global isotropic and radially anisotropic mantle structure including crustal thickness perturbations. J. Geophys. Res. 120, 4278–4300.
- Chanyshev, A., Ishii, T., Bondar, D., et al., 2022. Depressed 660-km discontinuity caused by akimotoite-bridgmanite transition. Nature 601, 69–73.
- Chase, C.G., Sprowl, D.R., 1983. The modern geoid and ancient plate boundaries. Eart.
- Chen, G., Cheng, Q., Zuo, R., Liu, T., Xi, Y., 2015. Identifying gravity anomalies caused by granitic intrusions in Nanling mineral district, China: a multifractal perspective. Geophys. Prosp. 63, 256–270.
- Chen, G., Cheng, Q., Zhang, H., 2016. Matched filtering method for separating magnetic anomaly using fractal model. Comput. Geosci. 90, 179–188.
- Connard, G., Couch, R., Gemperle, M., 1983. Analysis of aeromagnetic measurements from the Cascade Range in Central Oregon. Geophys. 48, 376–390.
- Dampney, C.N.G., 1969. The equivalent source technique. Geophys. 34 (1), 39-53.
- Dimri, V.P., 1992. Deconvolution and Inverse Theory. Elsevier, Amsterdam.
- Dimri, V.P., Bansal, A.R., 2021. Review of Scaling Approach to Estimate Depths from Gravity and magnetic Data. Jour. of Geol. Soc. of India 97, 1300–1306.
- Dimri, V.P., Ganguli, S.S., 2019. Fractal Theory and its Implication for Acquisition, Processing and Interpretation (API) of Geophysical Investigation: a Review. Jour. of Geol. Soc. of India 93 (2), 142–152.
- Fedi, M., 2016. Scaling Laws in Geophysics: Application to potential Fields of Methods based on the Laws of Self-similarity and Homogeneity. In: Dimri, V. (Ed.), Fractal Solutions for Understanding Complex Systems in Earth Sciences. Springer Earth System Sciences. Springer, Cham.
- Fedi, M., Quarta, T., Santis, A.D., 1997. Inherent power-law behavior of magnetic field power spectra from a Spector and Grant ensemble. Geophys. 62, 1143–1150.
- Förste, C., Bruinsma, S.L., Abrikosov, O., Lemoine, J.M., Charles, M.J., Flechtner, F., Balmino, G., Barthelmes, F., Biancale, R., 2014. EIGEN-6C4 the latest combined global gravity field model including GOCE data up to degree and order 2190 of GFZ Potsdam and GRGS Toulouse. GFZ Data Services. https://doi.org/10.5880/icgem.2015.1.
- Ganguli, S.S., Dimri, V.P., 2013. Interpretation of gravity data using eigenimage with Indian case study: a SVD approach. Jour. of App. Geophys. 95, 23–35.
- Garci'a-Abdeslem, J., Ness, G.E., 1994. Inversion of the power spectrum from magnetic anomalies. Geophy. 59, 391–401.
- Ghosh, A., Thyagarajulu, G., Steinberger, B., 2017. The Importance of Upper Mantle Heterogeneity in Generating the Indian Ocean Geoid Low. Geophy. Res. Lett. 44, 9707–9715.
- Gokul, V.S., Sreejith, K.M., Srinivasa Rao, G., Radhakrishna, M., Betts, P.G., 2022. Crustal and upper mantle density structure below the Indian Ocean Geoid Low based on 3-D constrained potential field modelling: Inferences on causative sources. Tectonophy. 822, 229161.
- Grand, S.P., 2002. Mantle shear-wave tomography and the fate of subducted slabs. Phil. Trans. Roy. Soc. Lond. A 360 (1800), 2475–2491.
- Gregotski, M.E., Jensen, O.G., Arkani-Hamed, J., 1991. Fractal stochastic modeling of aeromagnetic data. Geophys. 56, 1706–1715.
- Hager, B.H., 1984. Subducted slabs and the geoid: constraints on mantle rheology and flow. J. Geophys. Res. 89, 6003–6015.
- Hager, B.H., Richards, M.A., 1989. Long-wavelength variations in Earth's geoid: physical models and dynamical implications. Philos. Trans. R. Soc. Lond. Ser. A: Math. Phys. 521 202 203 207.
- Hosseini, K., Matthews, K.J., Sigloch, K., Shephard, G.E., Domeier, M., Tsekhmistrenko, M., 2018. SubMachine: Web-based tools for exploring seismic tomography and other models of Earth's deep interior. Geochem. Geophys. Geosyst.
- Ihnen, S.M., Whitcomb, J.H., 1983. The Indian Ocean gravity low: evidence for an isostatically uncompensated depression in the upper mantle. Geophy. Res. Lett. 10, 421-423
- Jenkins, J., Cottaar, S., White, R.S., Deuss, A., 2016. Depressed mantle discontinuities beneath Iceland: evidence of a garnet controlled 660 km discontinuity? Ear. Plan. Sc. Lett. 433, 159–168.
- Kelemework, Y., Fedi, M., Milano, M., 2021. A review of spectral analysis of magnetic data for depth estimation. Geophys. 86, J33–J58.
- Kumar, P., Yuan, X.H., Kumar, M.R., Kind, R., Li, X.Q., Chadha, R.K., 2007. The rapid drift of the Indian tectonic plate. Nature 449, 894–897.
- Lovejoy, S., Pecknold, S., Schertzer, D., 2001. Stratified multifractal magnetization and surface geomagnetic fields-I, Spectral analysis and modelling. Geophys. J. Int. 145, 112–126.
- Mandelbrot, B.B., 1982. The Fractal Geometry of Nature. W. H. Freeman and Company, New York, p. 480.

- Masters, G., Laske, G., Bolton, H., Dziewonski, A., 2000. The relative behavior of shear velocity, bulk sound speed, and compressional velocity in the mantle: Implications for chemical and thermal structure. In: Karato, S., et al. (Eds.), Earth's Deep Interior: Mineral Physics and Tomography from the Atomic to the Global Scale, Geophysical Monograph Series, vol. 117, p. 6387.
- Maus, S., Dimri, V.P., 1994. Scaling properties of potential fields due to scaling sources. Geophys. Res. Lett. 21, 891–894.
- Maus, S., Dimri, V.P., 1995. Potential field power spectrum inversion for scaling geology. Jour. Geophys. Res. 100, 12605–12616.
- Maus, S., Dimri, V.P., 1996. Depth estimation from the scaling power spectrum of potential field? Geophys. J. Int. 124, 113–120.
- Menke, W., 2012. Geophysical Data Analysis: Discrete Inverse Theory, 3rd ed. Elsevier, New York.
- Mishra, D.C., 2014. Geoid low and highs of the Indian Ocean and Western Pacific: Implications to mantle convection. J. Asian Earth Sci. 79, 441–445.
- Mishra, D.C., Ravi Kumar, M., 2012. Long and short wavelengths of Indian Ocean geoid and gravity lows: Mid-to-upper mantle sources, rapid drift and seismicity of Kachchh and Shillong plateau. India. Jour. of Asian Earth Sc. 60, 212–224.
- Naidu, P.S., 1972. Maximum likelihood (ML) estimation of depth from the spectrum of aeromagnetic fields. Pure Appl. Geophys. 95, 141–149.
- Negi, J.G., Pandey, O.P., Agarwal, P.K., 1987. Supermobility of hot Indian lithosphere. Tectonophy 135, 145–156.
- Negi, S.S., Kumar, A., Ningthoujam, L.S., Pandey, D.K., 2022. Mapping the mantle transition zone beneath the Indian Ocean geoid low from Ps receiver functions. Tectonophy. 831, 229330.
- Nerlich, R., Colli, L., Ghelichkhan, S., Schuberth, B., Bunge, H.P., 2016. Constraining central Neo-Tethys Ocean reconstructions with mantle convection models. Geophy. Res. Lett. 43, 9595–9603.
- Oliveira Jr., V.C., Barbosa, V.C.F., Uieda, L., 2013. Polynomial equivalent layer. Geophys. 78 (1), G1–G13.
- Pavlis, N.K., Holmes, S.A., Kenyon, S.C., Factor, J.K., 2012. The development and evaluation of the Earth Gravitational Model 2008 (EGM2008). J. Geophys. Res. 117, B04406
- Pawlowski, R.S., 1994. Green's equivalent-layer concept in gravity band-pass filter design. Geophys. 59 (1), 69–76.
- Pilkington, M., Todoeschuck, J.P., 1990. Stochastic inversion for scaling geology. Geophys. J. Int. 102, 205–217.
- Pilkington, M., Todoeschuck, J.P., 1993. Fractal magnetization of continental crust. Geophy. Res. Lett. 20, 627–630.
- Quarta, T., Fedi, M., Santis, A.D., 2000. Source ambiguity from an estimation of the scaling exponent of potential field power spectra. Geophys. Jour. Intl. 140 (2), 311–323.
- Rao, B.P., Kumar, M.R., 2014. Seismic evidence for slab graveyards atop the Core Mantle Boundary beneath the Indian Ocean Geoid Low. Phys. Earth Planet. Int. 236, 52–59.
- Rao, B.P., Kumar, M.R., Saikia, D., 2020. Seismic evidence for a hot mantle transition zone beneath the Indian Ocean Geoid Low. Geochem. Geophys. Geosyst. 21 (7) e2020GC009079.

Reid, A.B., Allsop, J.M., Granser, H., Millett, A.J., Somerton, I.W., 1990. Magnetic interpretation in three dimensions using Euler deconvolution. Geophys. 55, 80–91.

- Reiss, A., Thomas, C., Driel, J., Heyn, B., 2017. A hot midmantle anomaly in the area of the Indian Ocean geoid low. Geophy. Res. Lett. 44, 6702–6711.
- Ricard, Y., Fleitout, L., Froidevaux, C., 1984. Geoid heights and lithospheric stresses for a dynamic Earth. Ann. Geophys. 2, 267–286.
- Richards, M., Engebretson, D., 1992. Large-scale mantle convection and the history of subduction. Nat. 355, 437–440.
- Ritsema, J., Deuss, A., van Heijst, H.J., Woodhouse, J.H., 2011. S40RTS: a degree-40 shear velocity model for the mantle from new Rayleigh wave dispersion. Teleseismic traveltime and normal-mode splitting function measurements. Geophys. J. Int. 184 (3), 1223–1236.
- Ross, H.E., Blakely, R.J., Zoback, M.D., 2006. Testing the use of aeromagnetic data for the determination of Curie depth in California. Geophy. 71, L51.
- Rudolph, M.L., Lekić, V., Lithgow-Bertelloni, C., 2015. Viscosity jump in Earth's midmantle. Science 350, 1349–1352.
- Schlich, R., 1982. The Indian Ocean: Aseismic Ridges, Spreading Centers, and Oceanic Basins. In: Nairn, A.E.M., Stehli, F.G. (Eds.), The Ocean Basins and Margins. Springer, Boston, MA.
- Shahraki, M., Schmeling, H., Kaban, M.K., Petrunin, A.G., 2015. Effects of the postperovskite phase change on the observed geoid. Geophy. Res. Lett. 42 (1), 44–52.
- Simmons, N.A., Forte, A.M., Boschi, L., Grand, S.P., 2010. GyPSuM: a joint tomographic model of mantle density and seismic wave speeds. J. Geophys. Res. 115, B12310.
- Smith, W.H., Sandwell, D.T., 1997. Global Sea Floor Topography from Satellite Altimetry and Ship Depth Soundings. Science 277, 1956–1962.
- Spasojevic, S., Gurnis, M., Sutherland, R., 2010. Mantle upwellings above slab graveyards linked to the global geoid lows. Nat. Geosc. 3, 435–438.
- Spector, A., Grant, F.S., 1970. Statistical models for interpreting aeromagnetic data. Geophys. 35, 293–302.
- Stein, C., Stein, S., 1992. A model for the global variation in oceanic depth and heat flow with lithospheric age. Nature 359, 123–129.
- Steinberger, B., 2000. Slabs in the lower mantle—results of dynamic modeling compared with tomographic images and the geoid. Phys. Earth Planet. Inter. 118, 241–257.
- Steinberger, B., Calderwood, A.R., 2006. Models of large-scale viscous flow in the Earth's mantle with constraints from mineral physics and surface observations. Geophys. J. Int. 167, 1461–1481.
- Steinberger, B., Rathnayake, S., Kendall, E., 2021. The Indian Ocean Geoid Low at a plume-slab overpass. Tectonophy. 817, 229037.
- Suo, Y., Li, S., et al., 2021. Mantle micro-block beneath the Indian Ocean and its implications on the continental rift-drift-collision of the Tethyan evolution. Earth Sc. Rev. 217, 103622.
- Turcotte, D.L., 1992. Fractal and chaos in Geology and Geophysics. Cambridge Univ.
- Utsugi, M., 2019. 3-D inversion of magnetic data based on the L1–L2 norm regularization. Earth, Pl. Sp. 71, 73. https://doi.org/10.1186/s40623-019-1052-4.